



Cite this: *Phys. Chem. Chem. Phys.*,
2025, 27, 4804

Proton transport in liquid phosphoric acid: the role of nuclear quantum effects revealed by neural network potential[†]

Pei Liu, Wei Li * and Shuhua Li *

Pure phosphoric acid exhibits high proton conductivity and is widely used in modern industry. However, its proton transport mechanism remains less understood compared to that of water, which presents a significant challenge for advancing technologies like phosphoric acid fuel cells. In this study, we utilize machine learning potentials and molecular dynamics (MD) simulations to investigate the proton diffusion mechanisms in liquid phosphoric acid systems. The neural network potentials we developed demonstrate quantum chemical accuracy and stability across a range of temperatures. Our simulations reveal continuous proton hopping between phosphoric acid anions. Moreover, the radial distribution functions and diffusion coefficients obtained from ring polymer MD—a variant of path-integral MD—exhibit improved alignment with experimental values compared to classical MD results, as ring polymer MD inherently accounts for nuclear quantum effects on proton behavior. Additionally, we employed neural networks combined with the charge equilibration method to predict the charge distribution in liquid phosphoric acid, examining the proton transport mechanism through vibrational spectra analysis.

Received 3rd November 2024,
Accepted 10th February 2025

DOI: 10.1039/d4cp04195j

rsc.li/pccp

1. Introduction

Phosphoric acid, a widely used inorganic acid, plays a pivotal role in modern industry as an essential chemical substance.¹ It has attracted considerable attention across various disciplines, including atmospheric science,² environmental science,³ and astrophysics.⁴ Notably, phosphoric acid fuel cells represent the first generation of commercialized fuel cell technology.⁵ Due to its exceptional proton conductivity,^{6,7} pure phosphoric acid has found extensive application in energy technologies, such as proton exchange membrane fuel cells^{8–10} and phosphoric acid fuel cells.^{11,12} Additionally, phosphate-based systems are crucial in biological processes;¹³ the synthesis of adenosine triphosphate (ATP) is driven by proton concentration gradients between cellular compartments, with proton transport (PT) occurring near the surface of the phospholipid membrane.¹⁴ Therefore, investigating the physicochemical properties of phosphoric acid can provide valuable insights into the PT mechanisms in more complex materials and biological systems, underscoring its scientific importance.

Key Laboratory of Mesoscopic Chemistry of Ministry of Education, New Cornerstone Science Laboratory, School of Chemistry and Chemical Engineering, Nanjing University, Nanjing, Jiangsu 210023, People's Republic of China.

E-mail: shuhua@nju.edu.cn, wli@nju.edu.cn

† Electronic supplementary information (ESI) available. See DOI: <https://doi.org/10.1039/d4cp04195j>

To gain deeper insights into the properties and behavior of liquid phosphoric acid systems, molecular dynamics (MD) simulations are a commonly employed approach. Classical force fields (FFs), such as GROMOS¹⁵ and COMPASS,¹⁶ are typically used to explore the structural and dynamical properties of liquid phosphoric acid systems.^{17–19} These classical FFs can reproduce experimental radial distribution functions (RDFs) and densities,¹⁷ For example, Zhu *et al.* utilized classical FFs to investigate the microscopic structure and hydrogen bonding characteristics of pristine and phosphoric acid doped polybenzimidazoles.¹⁸ However, these classical FFs have precision limitations and are incapable of describing chemical reactions, making them inadequate for accurately modeling proton transfer processes in liquid phosphoric acid systems. In contrast, *ab initio* MD (AIMD) simulations are capable of describing chemical reactions with higher precision, providing detailed results such as vibrational spectra,²⁰ PT chains,⁶ and intermediate scattering functions²¹ of phosphoric acid. Nonetheless, the computational cost of AIMD scales significantly with system size, often limiting simulations to small systems and time scales of only a few ps.

To overcome these limitations and bridge the gap between efficiency and accuracy, various machine learning (ML) algorithms have been developed to construct FFs with *ab initio* accuracy by learning from reference *ab initio* data.^{22–27} ML potential (MLP)-based MD simulations combine the efficiency



of classical FF methods with the precision of AIMD.^{25,26,28–32} In these methods, the local atomic environment of each atom serves as the input, and the total energy of a large system is calculated by summing the atomic energy contributions, which depend on the local environment. Equivariant neural networks (NNs), such as NequIP,³³ Allegro,³⁴ and MACE,³⁵ are employed to construct equivariant interatomic potentials. These potentials rely on relative interatomic position vectors and higher-order geometric tensors, rather than just scalar distances or angles. This enables the network to capture more complex geometric relationships and exhibit both rotational and translational equivariance. Compared to conventional neural network potentials (NNPs), this results in superior predictive accuracy and significantly higher sample efficiency. Jinnouchi utilized ML potentials to conduct MD simulations of liquid phosphoric acid to investigate its proton conduction properties.³⁶ However, the obtained RDFs and diffusion coefficients showed discrepancies compared to experimental values. We attribute these discrepancies to the neglect of nuclear quantum effects (NQEs) associated with protons in the simulations, which have been shown in previous studies to significantly impact PT.^{37–39}

In this work, we combined path-integral MD (PIMD) with NNPs, based on hybrid density functional theory (DFT), to construct a dataset for liquid phosphoric acid at multiple temperatures. This dataset was then used to train NNPs for liquid phosphoric acid. We conducted classical Born–Oppenheimer MD, abbreviated as MD, simulations and ring polymer MD (RPMD)⁴⁰ simulations utilizing our NNP. The results indicate that the impact of NQEs is clearly observed due to the substantial presence of protons. These NQEs significantly influence the structure and atomic arrangement of liquid phosphoric acid, thereby affecting the RDFs. Proton diffusion coefficients in the RPMD simulations were higher than those in the MD simulations, as NQEs lower the energy barriers for PT in liquid phosphoric acid. Additionally, the simulated vibrational spectra revealed overlapping P–O peaks and a broad O–H peak, reflecting the presence of hydrogen-bonding networks in liquid phosphoric acid, which facilitates long-range PT.

2. Methodology and computational details

2.1 Liquid phosphoric acid models

All liquid phosphoric acid systems were modeled with unit cells under three-dimensional periodic boundary conditions (PBCs). First, we optimized the structure of gaseous phosphoric acid molecules at the PBE0/def2-SVP level of theory. Packmol software⁴¹ was used to randomly pack the optimized structures into cubic boxes. To simulate the diffusion behavior of liquid phosphoric acid at different temperatures, we generated three boxes of varying sizes, with densities derived from experimental and theoretical studies of liquid phosphoric acid at 298.15 K, 333.15 K, and 350.15 K (1.874 g cm^{−3}, 1.830 g cm^{−3}, and 1.804 g cm^{−3}, respectively).^{36,42,43} As shown in Fig. 1, each box contains 38 phosphoric acid molecules.

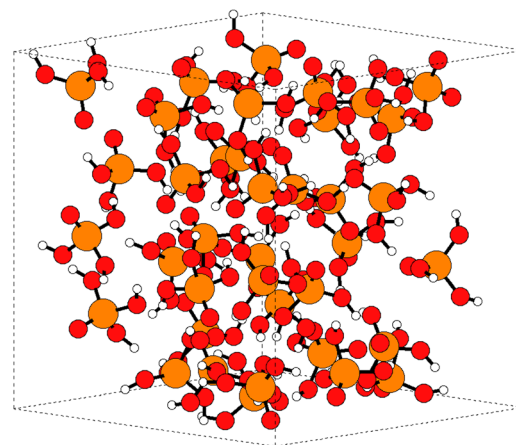


Fig. 1 Snapshot of a pure phosphoric acid system, containing 38 phosphoric acid molecules within the periodic cubic box. Red, orange, and white spheres represent oxygen, phosphorus, and hydrogen atoms, respectively.

To obtain equilibrium lattice structures, we employed the SCC-DFTB⁴⁴ semi-empirical method to optimize the three initial configurations and performed NVT MD simulations at 298.15 K, 333.15 K, and 350.15 K for 200 ps each using the CP2K software.⁴⁵ In the MD simulations, the time step was set to 1 fs for efficient structural relaxation. We randomly sampled 200 structures from the last 100 ps of each trajectory to create an initial dataset, which was then used to train preliminary NNs for subsequent active learning iterations.

2.2 Neural network potential generations

To construct a high-accuracy NNP for liquid phosphoric acid, we employed an active learning approach using committee NNs for iterative sampling.^{46,47} After each round of NNP training, we conducted MD simulations on three different initial structures at three temperatures under PBCs. The initial simulated trajectories lasted a few ps and were extended to 1 ns as the iterations increased. Configurations were extracted at 100 fs intervals during each sampling round as candidate samples. Four models were trained on the same dataset, forming the committee NNs. These committee NNs evaluated all candidate configurations by calculating the maximum standard deviation of atomic forces. Approximately 500 configurations with the largest force deviations were selected for further sampling. We then calculated the energy, atomic forces, and atomic charges of the selected configurations, adding these results to the dataset. This iterative process was repeated until the NNs converged on the test set.

Fig. 1 illustrates the periodic structure of liquid phosphoric acid in the dataset. All calculations in this study were performed at the Gamma point. Single-point calculations were carried out using the CP2K software with the mixed Gaussian and plane wave (GPW) method at the PBE0-D3(BJ)/TZVP-MOLOPT-GTH level.^{48–50} The auxiliary density matrix method (ADMM)⁵¹ was applied with admm-dzp as the auxiliary basis set. The Coulomb truncation of the hybrid functional was set to 6.0 Å, while the plane wave cutoff was established at 550



Rydberg, with convergence tests for the cutoff energy shown in Fig. S1 and Table S1 of the ESI.† Atomic charges were calculated using the Hirshfeld-I method.⁵²

The NN model used in this work is the MACE equivariant graph NN (GNN). In the MACE equivariant GNN, the interatomic graph comprises atomic nodes and edges connecting these atoms.^{35,53} An atom j near atom i is included in the graph if it is within the truncation radius r_{ij} , which is a hyperparameter of the NN. The features of node i are represented by $h_{i,kL}^{(t)}$, where t denotes the layer number, k indexes this series of features, which also corresponds to the number of chemical channels. L specifies the feature set of node i as well as the transformation of $h_{i,kL}^{(t)}$:

$$h_{i,kLM}^t(Q \cdot (r_1, \dots, r_N)) = \sum_{M'} D_{M'M}^L(Q) h_{i,kLM'}^t(r_1, \dots, r_N) \quad (1)$$

Here, $D^L(Q) \in \mathbb{R}^{(2L+1) \times (2L+1)}$ represents an L -th order Wigner D -matrix, and Q denotes a set of rotational transformations applied to atomic coordinates. When all features are labeled as $L = 0$, they represent invariant scalars. For $L > 0$, they correspond to tensors of the respective order: vectors for $L = 1$, matrices for $L = 2$, and higher-order tensors for larger values of L .

The network outputs the atomic energy E_A for each atom A based on the local environment descriptors of the atoms. The total energy E is the sum of the atomic energies in the system:

$$E = \sum_{A \in N_{\text{atom}}} E_A \quad (2)$$

The atomic force F_A on atom A is the negative gradient of the total energy with respect to the position of atom A .

The NNP developed for liquid phosphoric acid is termed PBE0-NN. Additionally, we combined the MACE model with the charge equilibration (Qeq) method to develop a NN for predicting the charge distribution within liquid phosphoric acid systems, termed Qeq-NN. In Qeq-NN, atomic charges are determined by minimizing a simplified energy expression:

$$Q = \arg \min \left[\sum_A \chi_A Q_A + \sum_A J_A Q_A^2 + E_{\text{coul}} - \lambda \left(\sum_A Q_A - Q_{\text{tot}} \right) \right] \quad (3)$$

Here, χ_A is the electronegativity of atom A , indicating its ability to attract electrons, and J_A denotes the hardness of atom A , reflecting the resistance of the molecule to charge fluctuations.⁵⁴ We interpret the electronegativity and hardness as environmentally dependent, learnable atomic properties. In eqn (3), the Coulomb potential E_{coul} is calculated using the reciprocal space term in the Ewald summation method:⁵⁵

$$E_{\text{coul}}(Q, R) = \frac{2\pi}{V} \sum_{A,B} Q_A Q_B \sum_{k \neq 0} \frac{\exp(-(k/2\alpha)^2 + ik \cdot (r_A - r_B))}{k^2} \quad (4)$$

Here, r_A is the position of particle A in real space, \mathbf{k} is the wave vector, $\alpha = 1/R_{\text{cutoff}}$ is the cutoff parameter for the Coulomb potential, with R_{cutoff} set to 2 Bohr. After training, the Qeq-NN can predict the electronegativity and hardness of all atoms in

Table 1 Hyperparameter settings for two MACE-equivariant GNNs

Model	Cutoff radius $r/\text{\AA}$	Chemical channels k	Max L
Qeq-NN	4.5	16	1
PBE0-NN	4.5	128	1

liquid phosphoric acid, which are then substituted into eqn (3) to calculate the atomic charge distribution. The loss functions for the two NNs, PBE0-NN and Qeq-NN, are defined as follows:

$$L_{\text{Qeq}} = \sqrt{\sum_i^m (Q_{\text{pred}} - Q_{\text{ref}})^2} \quad (5)$$

$$L_{\text{EF}} = \frac{w_E}{m} \sum_{i=1}^m |E_{\text{pred},i} - E_{\text{ref},i,\text{SR}}|^2 + \frac{w_F}{m} \sum_{i=1}^m \sum_A^{\text{Nat}} |F_{\text{pred},i,A} - F_{\text{ref},i,A}|^2 \quad (6)$$

The hyperparameters are provided in Table 1:

Following several rounds of active learning, the final dataset for liquid phosphoric acid comprised 4947 energies, 4 511 664 atomic forces, and 1503 888 atomic charges. This dataset was randomly split into a training set and a validation set with an 88% to 12% ratio and was used to train the MACE equivariant GNNs, PBE0-NN and Qeq-NN. The test set, consisting of 600 frames of periodic liquid phosphoric acid systems, was randomly sampled from all six trajectories, which included both MD and RPMD ones at three different temperatures.

We evaluated the predictive accuracy of the two NNs. For the test set, the correlation coefficient (R^2) between the atomic forces predicted by PBE0-NN and the reference values was 99.84% (see Fig. S3, ESI†), demonstrating excellent predictive performance. The mean absolute errors (MAEs) for energies and atomic forces were 0.238 meV per atom and 35.13 meV \AA^{-1} , respectively, closely aligned with the errors observed on the training and validation sets (see Table S2, ESI†). This consistency suggests that the NNP has achieved quantum chemical accuracy. Additionally, the MAE of atomic partial charge predictions in the periodic liquid phosphoric acid system, obtained using the Qeq-NN model, was as low as 0.003 e . This indicates that we can efficiently and accurately predict the distribution of partial charges throughout the trajectory, enabling precise analysis in subsequent trajectory studies. To assess the computational speed improvement of NNP MD simulations using PBE0-NN compared to AIMD, we tested systems of three different sizes (see in Fig. S4 and Table S4, ESI†). The results showed that our NNP achieved a performance efficiency improvement of at least 2400-fold over AIMD on CPU. Given that the NNP is deployed to run on GPUs, the computational efficiency in actual simulations is even more substantial. The computational resources for generating the dataset and training the ML model are compared in Section S3 of the ESI.†

2.3 Analysis methods

The trajectories obtained from MD simulations can be used to calculate the RDF, $g_{A-B}(r)$. The RDF describing the density of atoms of element B around atoms of element A and is defined



as follows:

$$gA\cdot B(r) = \frac{V}{N_A N_B} \left\langle \sum_{i \in A} \sum_{j \in B, j \neq i} \delta(r - r_{ij}) \right\rangle \frac{1}{4\pi r^2} \quad (7)$$

Here, N_A and N_B represent the number of atoms of element A and element B , respectively, and $\delta(r - r_{ij})$ is the Dirac delta function. The RPMD-simulated RDFs are obtained by statistically analyzing the structures of all beads. After obtaining the RDFs, the average coordination number (CN) n_A^B of atom A surrounded by atom B can be calculated from the integral of the RDFs over the spherical shell between intervals R_1 and R_2 :

$$n_A^B(R_1, R_2) = 4\pi \rho c_B \int_{R_1}^{R_2} gA\cdot B(r) r^2 dr \quad (8)$$

The diffusion of molecules and atoms in liquid phosphoric acid is crucial for understanding its transport properties. Given the strong PT capabilities of phosphoric acid under standard conditions, investigating the proton diffusion coefficient provides valuable insights into the mechanisms that facilitate efficient PT in liquid phosphoric acid. In condensed-phase systems, the diffusion coefficient for a specific atomic species can be derived from the slope of the mean square displacement (MSD) of the corresponding atoms:

$$MSD(t) = \frac{1}{N} \sum_{i=1}^N [r_i(t_0 + t) - r_i(t_0)]^2 \quad (9)$$

$$D = \frac{1}{6} \frac{d}{dt} MSD(t) \quad (10)$$

The vibrational density of states (VDOS) is a tool used in MD simulations to analyze the dynamic properties of a system. The VDOS can be calculated from the autocorrelation function of atomic velocities, $v_i(t)$, obtained from the MD trajectories:

$$I(\omega)_{PW} = \frac{1}{2\pi} \int \sum_i \delta v_i(t_0) \cdot \delta v_i(t_0 + t) e^{-i\omega t} dt \quad (11)$$

Here, $I(\omega)_{PW}$ represents the spectral density of the VDOS. After using Qeq-NN to predict the point charge distribution along the trajectory, we can calculate the dipole moment of the simulated system as follows:

$$M(t) = \sum_A Q_A(t) r_A(t) \quad (12)$$

Here, $Q_A(t)$ and r_A are the point charge and position of atom A at time t , respectively. Then, the infrared (IR) absorption intensity $I(\omega)_{IR}$ of the target system can be calculated through the time correlation function of the dipole moment $M(t)$:⁵⁶

$$I(\omega)_{IR} = \frac{1}{2\pi} \int \delta M(t_0) \cdot \delta M(t_0 + t) e^{-i\omega t} dt \quad (13)$$

The RPMD-simulated dynamical properties of liquid phosphoric acid are calculated by first averaging the coordinates, velocities, and dipole moments of different beads. These averaged values are then substituted into the corresponding formulas to obtain the desired dynamical properties.

2.4 Simulation details

We performed canonical ensemble MD simulations using the trained PBE0-NN model at three temperatures (298.15 K, 333.15 K, and 350.15 K) each for a duration of 1 ns. Additionally, we conducted canonical ensemble RPMD simulations with 12 beads at the same three temperatures for 100 ps, utilizing the PBE0-NN to explore NQEs in the phosphoric acid system. All NNP-based MD and RPMD simulations were performed with the i-PI software.^{57,58} For comparison, we also carried out a CVFF-based⁵⁹ MD simulation of phosphoric acid at 298.15 K starting from the same initial structure and applying identical MD simulation parameters with the LAMMPS software.⁶⁰ A Langevin thermostat⁶¹ was used to control the temperature in all MD simulations in this work. The computational resources for simulations and DFT calculations are compared in Section S3 of the ESI.†

3. Results and discussions

3.1 Radial distribution functions

To verify the accuracy of the PBE0-NN MD simulation trajectories and to characterize the simulated structural information, we calculated the RDFs from the MD simulations of the phosphoric acid system and compared the results with those obtained from neutron scattering experiments,⁴³ as shown in Fig. 2 and Table 2. It should be mentioned that all experimental data presented in our study were obtained using pure phosphoric acid.

Fig. 2 illustrates that the PBE0-NN MD results align closely with experimental RDFs, particularly in terms of peak positions for gX-X, gH-X, and gH-H in the phosphoric acid system. However, there are some discrepancies in the shape and intensity of these peaks. The first peak in gX-X, located at 1.57 Å in the PBE0-NN MD simulations, corresponds to the P-O bond within the phosphoric acid molecule and shows a minor deviation of 0.03 Å from the experimental value. In gas-phase phosphoric acid, P-O bonds are classified into single bonds (1.60 Å) and double bonds (1.46 Å).²⁰ In the condensed-phase phosphoric acid system, however, only a single peak appears in the RDFs due to the influence of a strong hydrogen-bonding network. The second peak in gX-X, at 2.55 Å, represents O-O intramolecular correlations, with a 0.04 Å deviation from the experimental value. Overall, the deviations between PBE0-NN MD-simulated and experimental gX-X peak positions are small. Additionally, there is little difference between RPMD and MD results for gX-X, as NQEs are less significant for heavier atoms like O and P.

The gH-X peaks from both MD and RPMD simulations are similarly positioned and closely match experimental values. The first peak at 1.00 Å in gH-X corresponds to the covalent O-H bond, with a deviation of only 0.02 Å from the experimental value. RPMD simulations provide a more accurate depiction of peak intensity and width compared to MD. The second peak in gH-X, located at 1.53 Å, represents the intermolecular O-H-O hydrogen bond, deviating by 0.01 Å from the experimental value.



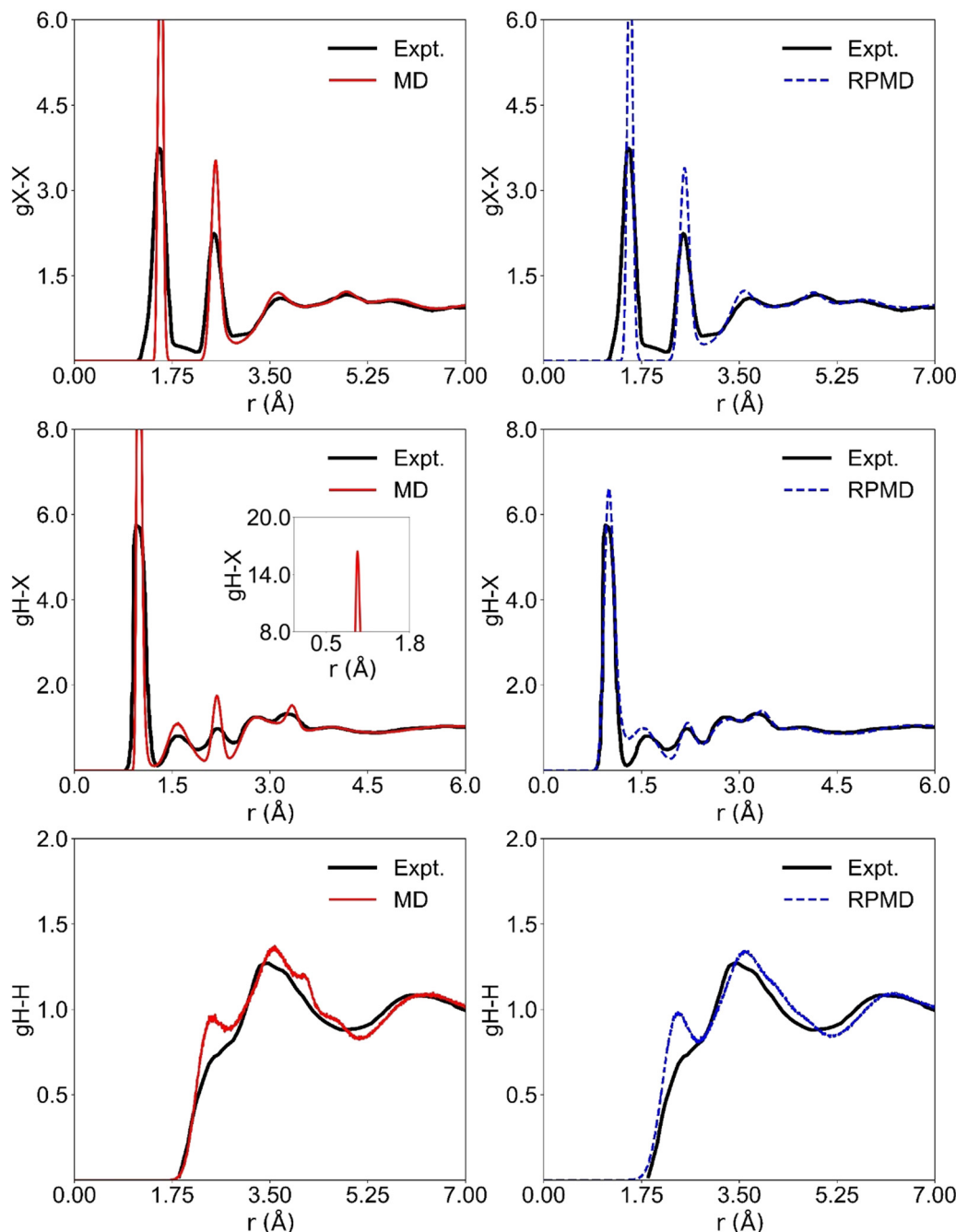


Fig. 2 Radial distribution function of the phosphoric acid system at 333.15 K, obtained from PBE0-NN MD and RPMD simulations, compared with the experimental data.⁴³ The variable X represents oxygen (O) and phosphorus (P) atoms.

The overlap of these two peaks in $gH\text{-}X$ suggests frequent proton transfers along strong $\text{O}\cdots\text{H}\text{-O}$ hydrogen bonds in liquid phosphoric acid. However, RPMD might slightly overestimate this overlap compared to experimental data. The third and fourth peaks in $gH\text{-}X$ reflect non-bonded intramolecular $\text{H}\text{-P}$ and $\text{H}\text{-O}$ interactions, respectively, with RPMD providing a significantly better representation of these interactions than MD.

The first peak in $gH\text{-H}$, spanning 1.90 to 2.60 Å, captures $\text{H}\text{-H}$ correlations across adjacent hydrogen bonds. The MD simulations, however, tend to overestimate the intensity of this peak,

indicating that the hydrogen-bond network in phosphoric acid appears more structured in simulations than in experimental measurements. Nonetheless, the $gH\text{-H}$ peaks from both MD and RPMD simulations qualitatively agree with experimental data.

As presented in Table 2, the average coordination numbers calculated (CNs) from RPMD and MD simulations show no significant differences, indicating that PBE0-NN accurately predicts the structure and local atomic environment of phosphoric acid. Furthermore, the $gH\text{-X}$ RDFs in Fig. 2 reveal that RPMD, which accounts for NQE, produces RDFs with peak



Table 2 Peak types, positions, and average coordination numbers (CNs) of the phosphoric acid system at 333.15 K, obtained from PBE0-NN MD and RPMD simulations

Peak ^a	Position/Å	Average CNs ^b	Assignment
gX-X (1)	1.57 (1.54)	1.10/1.19 (1.16)	P–O bonds
gX-X (2)	2.55 (2.51)	3.80/3.84 (3.82)	O–O intramolecular
gH-X (1)	1.00 (0.98)	0.95/0.95 (0.95)	H–O bonds
gH-X (2)	1.53 (1.54)	0.73/0.76 (0.75)	H–O through hydrogen bonds
gH-X (3)	2.20 (2.20)	n.m.	H–P intramolecular
gH-X (4)	2.80 (2.80)	n.m.	H–O intramolecular
gH-H (1)	1.90–2.60	n.m.	H–H across hydrogen bond
gH-H (2)	2.60–4.10	n.m.	H–H intramolecular and intermolecular

^a Peak labels as shown in Fig. 2, where X represents O and P atoms. ^b Values presented before and after the slash correspond to MD and RPMD simulations, respectively. Experimental values of pure phosphoric acid from ref. 43 are provided in parentheses. n.m.: not meaningful.

intensities and shapes that are more consistent with experimental values. The overlap of the O–H bond and O···H–O hydrogen bond peaks suggests a lower energy barrier for proton transfer between oxygen atoms, potentially indicating increased proton diffusion and hopping in RPMD simulations. This aspect will be explored in the following section.

3.2 Proton diffusion

Fig. 3 illustrates the snapshots extracted from PBE0-NN MD trajectories at 298.15 K. These four panels sequentially display the transfer of three protons along a hydrogen bond chain to new oxygen atoms. Fig. 3(a) shows the initial 0 ps snapshot, where four phosphoric acid molecules or ions form a chain-like structure stabilized by hydrogen bonds. According to the Grotthuss mechanism,⁶² protons are transported through this hydrogen bond network by the continuous breaking and reforming of hydrogen bonds. Fig. 3(b) illustrates a later snapshot in which a proton (highlighted in yellow) has transferred from one oxygen atom to another along the hydrogen bond. About 3 ps later, as shown in Fig. 3(c), a second proton

undergoes a similar transfer. Four ps after that, a third proton transfer occurs, depicted in Fig. 3(d).

According to previous studies,²¹ proton transfer predominantly occurs through the hydrogen bond network rather than a molecular vehicle, as illustrated in Fig. 3. To investigate this, we tracked the motion of a single proton. Fig. 4 depicts its bonding to various oxygen atoms over time, excluding transfers to the same oxygen atom to provide a clearer view of directional PT within the hydrogen bond network. The transport distance of this proton is approximately 2 Å, contributing significantly to the high conductivity observed in liquid phosphoric acid.

Fig. 5 compares the proton diffusion coefficients at different temperatures from both PBE0-NN MD simulations and experimental data, with specific values listed in Table 3. The diffusion coefficients from the PBE0-NN MD simulations show a clear upward trend with increasing temperature. In RPMD simulations, the diffusion coefficients exhibit an exponential increase with temperature, aligning well with the experimental results.

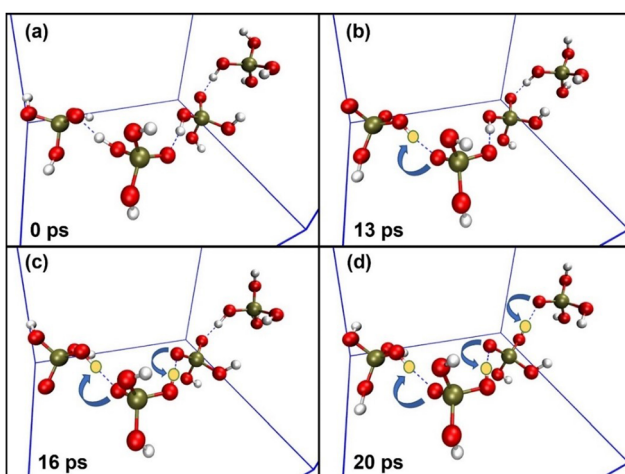


Fig. 3 Proton transport (PT) mechanism in the phosphoric acid system, illustrated through snapshots of PT chains in liquid phosphoric acid at 0 ps (a), 13 ps (b), 16 ps (c), and 20 ps (d) in the PBE0-NN MD trajectory at 298.15 K. Periodic boundaries, transported protons, and hydrogen bonds are represented by blue solid lines, yellow spheres, and green dashed lines, respectively.

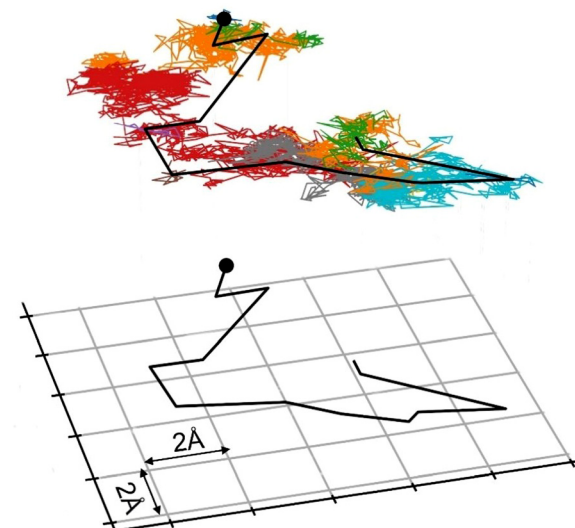


Fig. 4 Motion of a single proton in phosphoric acid obtained from PBE0-NN MD simulations at 298.15 K. The trajectory color changes each time the proton transfers to a different oxygen atom. A black line connects the center of mass of each proton cloud, projected onto the x–y plane for clarity.



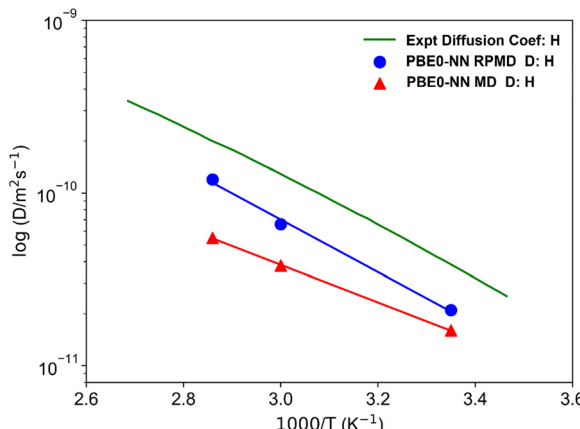


Fig. 5 Comparison of proton diffusion coefficients in the phosphoric acid system obtained from PBE0-NN MD and RPMD simulations at various temperatures, alongside experimental values of pure phosphoric acid from ref. 63.

Table 3 also reveals that the diffusion coefficient of P is much smaller than that of H. This supports the conclusion that PT in phosphoric acid primarily follows a hopping mechanism, consistent with the mechanism shown in Fig. 3. The differences between simulated and experimental diffusion coefficients are within an order of magnitude. At temperatures of 298.15 K, 333.15 K, and 350.15 K, experimental diffusion coefficients for hydrogen in phosphoric acid were determined to be $0.40 \times 10^{-10} \text{ m}^2 \text{ s}^{-1}$, $1.27 \times 10^{-10} \text{ m}^2 \text{ s}^{-1}$, and $2.02 \times 10^{-10} \text{ m}^2 \text{ s}^{-1}$, respectively. Corresponding MD values were $0.16 \times 10^{-10} \text{ m}^2 \text{ s}^{-1}$, $0.38 \times 10^{-10} \text{ m}^2 \text{ s}^{-1}$, and $0.55 \times 10^{-10} \text{ m}^2 \text{ s}^{-1}$, while RPMD values were $0.21 \times 10^{-10} \text{ m}^2 \text{ s}^{-1}$, $0.66 \times 10^{-10} \text{ m}^2 \text{ s}^{-1}$, and $1.20 \times 10^{-10} \text{ m}^2 \text{ s}^{-1}$. Similar to previous simulations of liquid water systems, RPMD results show enhanced hydrogen diffusion coefficients compared to MD, highlighting the significant impact of NQEs on phosphoric acid dynamics. Both RPMD and MD simulations predict lower diffusion coefficients than the experimental values at corresponding temperatures. As shown in Fig. 2, the first H-H peak intensities predicted by both MD and RPMD simulations are higher than experimental observations, which suggests that this discrepancy does not arise from the neglect of NQEs in the MD simulations. Similar discrepancy have been observed in previous PBE-based AIMD simulations of liquid phosphoric acid systems.²⁰ This discrepancy may stem from the inherent

Table 3 Diffusion coefficients (D) for H and P atoms obtained from PBE0-NN MD and RPMD simulations, as well as experimental data, at temperatures of 298.15 K, 333.15 K, and 350.15 K^a

Temperature/K	$D/10^{-10} \text{ m}^2 \text{ s}^{-1}$	
	H	P
298.15	0.16/0.21 (0.40)	0.04/0.06 (0.09)
333.15	0.38/0.66 (1.27)	0.06/0.22 (0.21)
350.15	0.55/1.20 (2.02)	0.11/0.39 (0.57)

^a Values presented before and after the slash correspond to MD and RPMD simulations, respectively. Experimental values of pure phosphoric acid from ref. 63 are provided in parentheses.

limitations of the DFT method, as several studies have pointed out that DFT often struggles to accurately predict hydrogen bonding and tends to underperform relative to more advanced methods like MP2.^{64,65} This effect could result in protons becoming “trapped” in the simulations, leading to slower diffusion than in experiments, where additional bond-breaking and reforming events enhance proton mobility.

Fig. 2 also shows that the RDFs for hydrogen bonds and covalent bonds exhibit greater overlap in RPMD than in MD. This overlap lowers the energy barrier for proton hopping between oxygen atoms, facilitating proton diffusion. In contrast, MD predicts sharper, more intense RDF peaks for covalent bonds, hydrogen bonds, and H-O and H-P correlations, reflecting a denser phosphoric acid configuration that restricts proton mobility. By incorporating NQE, RPMD provides a more accurate representation of these interactions, which is crucial for capturing proton dynamics in phosphoric acid.

3.3 Vibrational spectra

We compared the VDOS and IR spectra of phosphoric acid at 298.15 K from MD simulations with experimental data, as shown in Fig. 6 and 7. Fig. 6 shows the PBE0-NN MD simulated VDOS for phosphoric acid along with experimental Raman peaks at 298.15 K.⁶⁶ In Fig. 6(a), the MD-simulated VDOS does not display distinct vibrational peaks in the low- and mid-frequency regions. By contrast, Fig. 6(b) shows the VDOS from RPMD simulations, which features three distinct peaks, with those at 496 cm^{-1} and 359 cm^{-1} closely aligning with experimental observations. This alignment suggests that incorporating NQEs enhances the accuracy of vibrational energy spacing, evidenced by the sharper, more defined peaks in the RPMD spectrum. The simulated peak for P-O single bond stretching at 910 cm^{-1} matches the experimental value well in both MD and RPMD simulations, though the P-O double bond stretching exhibits a blue shift of approximately 100 cm^{-1} . The overlapping vibrations of P-O single and double bonds, due to frequent proton transfers within phosphate, obscure distinct spectral features. While no discrete O-H bond stretching peaks were observed in the experimental Raman spectra, the simulations reveal a broad peak between 2400 and 4000 cm^{-1} , significantly red-shifted compared to the sharp O-H stretching peak seen in gas-phase phosphoric acid.²⁰ This broadening and red shift can be attributed to strong hydrogen bonding in liquid phosphoric acid, which weakens the O-H bond and suppresses a well-defined stretching mode.

Fig. 7 illustrates the IR spectra for phosphoric acid at 298.15 K, as predicted by PBE0-NN and CVFF MD simulations, compared with experimental attenuated total reflectance IR spectra.⁶⁷ In the 400 – 1400 cm^{-1} region, the classical CVFF predicts two absorption peaks: one at 460 cm^{-1} with greater intensity than the 915 cm^{-1} peak. However, these peaks differ significantly from experimental data in terms of frequency, shape, and intensity. In contrast, PBE0-NN simulations, both MD and RPMD, produce an absorption peak at 490 cm^{-1} that closely matches the experimental peak in both frequency and shape. The experimental peak at 915 cm^{-1} , associated with P-O



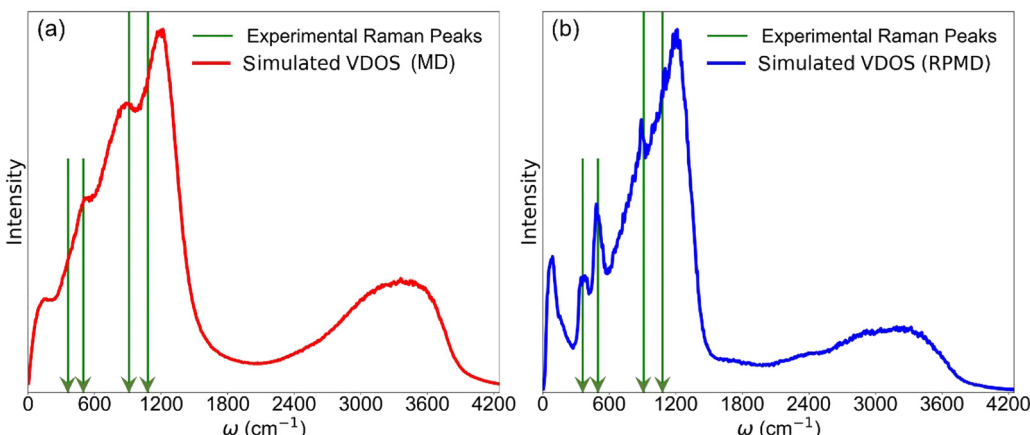


Fig. 6 Comparison of the VDOS predicted by PBE0-NN MD (a) and RPMD (b) simulations with experimentally observed vibrational frequencies of pure phosphoric acid from ref. 66. Green arrows indicate vibrational frequencies observed in the experimental Raman spectra of liquid phosphoric acid.

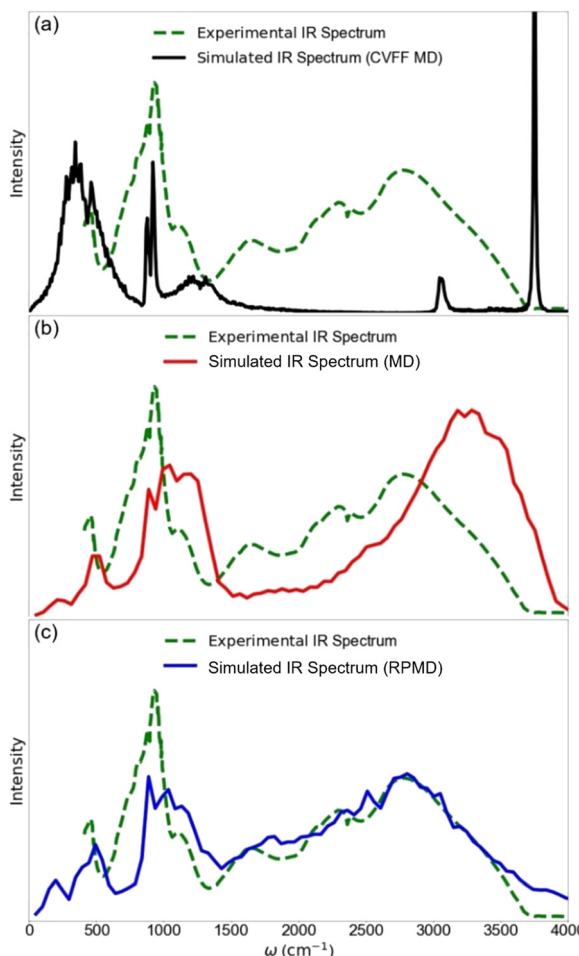


Fig. 7 Comparison of the IR spectra of pure phosphoric acid predicted by PBE0-NN MD and RPMD, and CVFF MD simulations with experimental data of pure phosphoric acid from ref. 67.

bond vibrations, is more intense than in PBE0-NN simulations, with the RPMD-predicted peak exhibiting a red shift of about

Table 4 Comparison of vibrational peak wavenumbers (cm^{-1}) from IR spectra: PBE0-NN MD and RPMD, and CVFF MD simulations versus experimental measurements of pure phosphoric acid from ref. 67

Peaks	Experiment	PBE0-NN RPMD	PBE0-NN MD	CVFF MD
1	470	490	490	460
2	915	885	1030	915
3	2780	2800	3270	3060/3750

30 cm^{-1} , bringing it closer to the experimental frequency (Table 4).

At high frequencies, the PBE0-NN simulations produce a broad absorption band from 2000 to 3800 cm^{-1} , consistent with the experimentally observed broad peak. In contrast, absorption peaks from classical FF are much narrower, showing two distinct peaks that fail to capture the complex hydrogen-bonding network in phosphates. The PBE0-NN method weakens the O-H bond force constant and enhances dipole moment changes during vibration, leading to broader, stronger absorption features. Specifically, PBE0-NN MD simulations reveal a prominent absorption peak at 3270 cm^{-1} , which is blue-shifted by approximately 490 cm^{-1} from the experimental value. In comparison, PBE0-NN RPMD, which accounts for NQEs of light atoms such as hydrogen, predicts O-H stretching peaks in the range of 2000 to 3500 cm^{-1} . The shape and intensity of this RPMD-predicted peak align well with experimental data, with only a 20 cm^{-1} blue shift at the peak's maximum.

These findings underscore the critical role of NQEs in influencing proton vibrational properties in liquid phosphoric acid. Classical MD, which neglects NQEs, underestimates the impact of strong hydrogen bonding on O-H vibrations in liquid phosphoric acid. In contrast, RPMD effectively captures these effects by modeling protons as a series of "beads" forming a ring polymer. Overall, these results highlight the strong predictive performance of the PBE0-NN method for the vibrational spectra of phosphoric acid and emphasize the indispensable

role of NQEs in facilitating PT within liquid phosphoric acid systems.

4. Conclusion

In this work, we developed a NNP for phosphoric acid based on a high-precision dataset generated using the PBE0 hybrid functional. Long-time simulations were conducted at three temperatures using both RPMD and MD simulations. The simulated RDFs closely align with experimental results, validating that the PBE0-NN model accurately captures the structural characteristics of phosphoric acid. Notably, the $g_{\text{H-X}}$ curves from RPMD match experimental data more closely than those from MD, highlighting the significant impact of NQEs on structural properties. Furthermore, analysis of the MD trajectories reveals continuous directional proton transfer along hydrogen-bond networks, indicating that PT in phosphoric acid follows the Grotthuss mechanism (similar to liquid water), where protons hopping through hydrogen bond breaking and reformation.

Comparing proton diffusion coefficients obtained from RPMD and MD at various temperatures confirmed that NQEs significantly enhance PT. Additionally, RPMD reproduces the vibrational density of states and IR spectra with greater accuracy in both shape and frequency. Our results show that RPMD not only provides more accurate vibrational energy spacing but also captures the effects of strong hydrogen bonding and proton tunneling on the transport and vibrational properties of phosphoric acid. These findings offer valuable insights and a robust foundation for further exploration of NQEs in the conductive properties of phosphoric acid and related materials. Building on this work, future research could explore the integration of NNP and PIMD simulations with low-scaling electron correlation methods.⁶⁸ This would enable the construction of datasets at the MP2 or CCSD(T) level, thus achieving more accurate NNP-based MD simulations. Additionally, we aim to develop NNs capable of predicting system pressure, which will enable pressure-controlled simulations. This approach will allow us to simulate the viscosity of phosphoric acid and phosphate systems across a range of temperatures and concentrations, thus providing a more comprehensive theoretical framework for understanding their properties.

Data availability

The data that support the findings of this study are available from the corresponding author upon reasonable request.

Conflicts of interest

There are no conflicts to declare.

Acknowledgements

This work was supported by the National Natural Science Foundation of China (grant no. 22273038, 22033004), Jiangsu Province Innovation Support Program (Soft Science Research)

Special Funding (no. BK20232012), and Nanjing University AI&AI for Science Special Project.

References

- 1 R. Gilmour, *Purification, Uses, Technology and Economics*, USA, 2013, pp.11–12.
- 2 J. Elm, N. Myllys and T. Kurtén, *Mol. Phys.*, 2017, **115**, 2168–2179.
- 3 M. Zeng, B. Liao, M. Lei, Y. Zhang, Q. Zeng and B. Ouyang, *J. Environ. Sci.*, 2008, **20**, 75–79.
- 4 M. Millan, S. Teinturier, C. A. Malespin, J. Y. Bonnet, A. Buch, J. P. Dworkin, J. L. Eigenbrode, C. Freissinet, D. P. Glavin, R. Navarro-González, A. Srivastava, J. C. Stern, B. Sutter, C. Szopa, A. J. Williams, R. H. Williams, G. M. Wong, S. S. Johnson and P. R. Mahaffy, *Nat. Astron.*, 2022, **6**, 129–140.
- 5 H. Abdi, R. Rasouli Nezhad and M. Salehimaleh, in *Distributed Generation Systems*, ed. G. B. Gharehpetian and S. M. Mousavi Agah, Butterworth-Heinemann, 2017, pp. 221–300.
- 6 L. Vilčiauskas, M. E. Tuckerman, G. Bester, S. J. Paddison and K.-D. Kreuer, *Nat. Chem.*, 2012, **4**, 461–466.
- 7 K.-D. Kreuer, *Chem. Mater.*, 1996, **8**, 610–641.
- 8 Q. Li, J. O. Jensen, R. F. Savinell and N. J. Bjerrum, *Prog. Polym. Sci.*, 2009, **34**, 449–477.
- 9 K. H. Lim, I. Matanovic, S. Maurya, Y. Kim, E. S. De Castro, J.-H. Jang, H. Park and Y. S. Kim, *ACS Energy Lett.*, 2023, **8**, 529–536.
- 10 G. Skorikova, D. Rauber, D. Aili, S. Martin, Q. Li, D. Henkensmeier and R. Hempelmann, *J. Membr. Sci.*, 2020, **608**, 118188.
- 11 H. R. Kim, J. H. Lee and T. S. Kim, *J. Mech. Sci. Technol.*, 2020, **34**, 3863–3874.
- 12 S. V. Kanuri and S. Motupally, in *Fuel Cells and Hydrogen Production: A Volume in the Encyclopedia of Sustainability Science and Technology*, ed. T. E. Lipman and A. Z. Weber, Springer, New York, New York, NY, 2nd edn, 2019, pp. 515–530.
- 13 F. H. Westheimer, *Science*, 1987, **235**, 1173–1178.
- 14 J. Heberle, J. Riesle, G. Thiedemann, D. Oesterhelt and N. A. Dencher, *Nature*, 1994, **370**, 379–382.
- 15 W. F. van Gunsteren and H. J. C. Berendsen, *Biochem. Soc. Trans.*, 1987, **15**, 303–306.
- 16 H. Sun, P. Ren and J. Fried, *Comput. Theor. Polym. Sci.*, 1998, **8**, 229–246.
- 17 S. A. H. Spieser, B. R. Leeflang, L. M. J. Kroon-Batenburg and J. Kroon, *J. Phys. Chem. A*, 2000, **104**, 7333–7338.
- 18 S. Zhu, L. Yan, D. Zhang and Q. Feng, *Polymer*, 2011, **52**, 881–892.
- 19 S. Li, J. R. Fried, J. Sauer, J. Colebrook and D. S. Dudis, *Int. J. Quantum Chem.*, 2011, **111**, 3212–3229.
- 20 E. Tsuchida, *J. Phys. Soc. Jpn.*, 2006, **75**, 054801.
- 21 I. Popov, Z. Zhu, A. R. Young-Gonzales, R. L. Sacci, E. Mamontov, C. Gainaru, S. J. Paddison and A. P. Sokolov, *Commun. Chem.*, 2023, **6**, 77.
- 22 M. Sun, A. W. Dougherty, B. Huang, Y. Li and C. H. Yan, *Adv. Energy Mater.*, 2020, **10**, 1903949.



23 V. L. Deringer, M. A. Caro and G. Csányi, *Adv. Mater.*, 2019, **31**, 1902765.

24 T. C. Ricard, X. Zhu and S. S. Iyengar, *J. Chem. Theory Comput.*, 2023, **19**, 8541–8556.

25 Z. Yan, D. Wei, X. Li and L. W. Chung, *Nat. Commun.*, 2024, **15**, 4181.

26 J. Liu, J. Lan and X. He, *J. Phys. Chem. A*, 2022, **126**, 3926–3936.

27 Y. Chen, Y. Ou, P. Zheng, Y. Huang, F. Ge and P. O. Dral, *J. Chem. Phys.*, 2023, **158**, 074103.

28 O. T. Unke and M. Meuwly, *J. Chem. Theory Comput.*, 2019, **15**, 3678–3693.

29 J. Zeng, D. Zhang, D. Lu, P. Mo, Z. Li, Y. Chen, M. Rynik, L. A. Huang, Z. Li, S. Shi, Y. Wang, H. Ye, P. Tuo, J. Yang, Y. Ding, Y. Li, D. Tisi, Q. Zeng, H. Bao, Y. Xia, J. Huang, K. Muraoka, Y. Wang, J. Chang, F. Yuan, S. L. Bore, C. Cai, Y. Lin, B. Wang, J. Xu, J.-X. Zhu, C. Luo, Y. Zhang, R. E. A. Goodall, W. Liang, A. K. Singh, S. Yao, J. Zhang, R. Wentzcovitch, J. Han, J. Liu, W. Jia, D. M. York, W. E. R. Car, L. Zhang and H. Wang, *J. Chem. Phys.*, 2023, **159**, 054801.

30 J. S. Smith, O. Isayev and A. E. Roitberg, *Chem. Sci.*, 2017, **8**, 3192–3203.

31 A. P. Bartók, M. C. Payne, R. Kondor and G. Csányi, *Phys. Rev. Lett.*, 2010, **104**, 136403.

32 J. Daru, H. Forbert, J. Behler and D. Marx, *Phys. Rev. Lett.*, 2022, **129**, 226001.

33 S. Batzner, A. Musaelian, L. Sun, M. Geiger, J. P. Mailoa, M. Kornbluth, N. Molinari, T. E. Smidt and B. Kozinsky, *Nat. Commun.*, 2022, **13**, 2453.

34 A. Musaelian, S. Batzner, A. Johansson, L. Sun, C. J. Owen, M. Kornbluth and B. Kozinsky, *Nat. Commun.*, 2023, **14**, 579.

35 I. Batatia, D. P. Kovacs, G. Simm, C. Ortner and G. Csányi, *NeurIPS*, 2022, **35**, 11423–11436.

36 R. Jinnouchi, *Phys. Chem. Chem. Phys.*, 2022, **24**, 15522–15531.

37 Y. Kawashima, K. Sawada, T. Nakajima and M. Tachikawa, *J. Comput. Chem.*, 2019, **40**, 172–180.

38 M. Heres, Y. Wang, P. J. Griffin, C. Gainaru and A. P. Sokolov, *Phys. Rev. Lett.*, 2016, **117**, 156001.

39 Y. Nishimura and H. Nakai, *J. Chem. Phys.*, 2023, **158**, 164101.

40 F. Paesani, W. Zhang, D. A. Case, T. E. Cheatham, III and G. A. Voth, *J. Chem. Phys.*, 2006, **125**, 184507.

41 L. Martínez, R. Andrade, E. G. Birgin and J. M. Martínez, *J. Comput. Chem.*, 2009, **30**, 2157–2164.

42 N. C. f. B. Information, PubChem Compound Summary for CID 1004, Phosphoric Acid., <https://pubchem.ncbi.nlm.nih.gov/compound/Phosphoric-Acid>, (accessed July 25, 2024).

43 R. H. Tromp, S. H. Spieser and G. W. Neilson, *J. Chem. Phys.*, 1999, **110**, 2145–2150.

44 M. Elstner, D. Porezag, G. Jungnickel, J. Elsner, M. Haugk, T. Frauenheim, S. Suhai and G. Seifert, *Phys. Rev. B: Condens. Matter Mater. Phys.*, 1998, **58**, 7260.

45 T. D. Kühne, M. Iannuzzi, M. Del Ben, V. V. Rybkin, P. Seewald, F. Stein, T. Laino, R. Z. Khalilullin, O. Schütt, F. Schiffmann, D. Golze, J. Wilhelm, S. Chulkov, M. H. Bani-Hashemian, V. Weber, U. Borštník, M. Taillefumier, A. S. Jakobovits, A. Lazzaro, H. Pabst, T. Müller, R. Schade, M. Guidon, S. Andermatt, N. Holmberg, G. K. Schenter, A. Hehn, A. Bussy, F. Belleflamme, G. Tabacchi, A. Glöß, M. Lass, I. Bethune, C. J. Mundy, C. Plessl, M. Watkins, J. VandeVondele, M. Krack and J. Hutter, *J. Chem. Phys.*, 2020, **152**, 194103.

46 C. Schran, K. Brezina and O. Marsalek, *J. Chem. Phys.*, 2020, **153**, 104105.

47 C. Schran, F. L. Thiemann, P. Rowe, E. A. Müller, O. Marsalek and A. Michaelides, *Proc. Natl. Acad. Sci. U. S. A.*, 2021, **118**, e2110077118.

48 C. Adamo and V. Barone, *J. Chem. Phys.*, 1999, **110**, 6158–6170.

49 L. Goerigk, A. Hansen, C. Bauer, S. Ehrlich, A. Najibi and S. Grimme, *Phys. Chem. Chem. Phys.*, 2017, **19**, 32184.

50 F. Weigend and R. Ahlrichs, *Phys. Chem. Chem. Phys.*, 2005, **7**, 3297.

51 M. Guidon, J. Hutter and J. VandeVondele, *J. Chem. Theory Comput.*, 2010, **6**, 2348–2364.

52 P. Bultinck, C. Van Alsenoy, P. W. Ayers and R. Carbó-Dorca, *J. Chem. Phys.*, 2007, **126**, 144111.

53 D. P. Kovács, J. H. Moore, N. J. Browning, I. Batatia, J. T. Horton, V. Kapil, I.-B. Magdäu, D. J. Cole and G. Csányi, *arXiv*, 2023, preprint, arXiv:2312.15211, DOI: [10.48550/arXiv.2312.15211](https://doi.org/10.48550/arXiv.2312.15211).

54 W. Kohn, A. D. Becke and R. G. Parr, *J. Phys. Chem.*, 1996, **100**, 12974–12980.

55 A. Y. Toukmaji and J. A. Board, *Comput. Phys. Commun.*, 1996, **95**, 73–92.

56 V. Agarwal, G. W. Huber, W. C. Conner, Jr. and S. M. Auerbach, *J. Chem. Phys.*, 2011, **135**, 134506.

57 V. Kapil, M. Rossi, O. Marsalek, R. Petraglia, Y. Litman, T. Spura, B. Cheng, A. Cuzzocrea, R. H. Meißner, D. M. Wilkins, B. A. Helfrech, P. Juda, S. P. Bienvenue, W. Fang, J. Kessler, I. Poltavsky, S. Vandenbrande, J. Wieme, C. Corminboeuf, T. D. Kühne, D. E. Manolopoulos, T. E. Markland, J. O. Richardson, A. Tkatchenko, G. A. Tribello, V. Van Speybroeck and M. Ceriotti, *Comput. Phys. Commun.*, 2019, **236**, 214–223.

58 M. Ceriotti, J. More and D. E. Manolopoulos, *Comput. Phys. Commun.*, 2014, **185**, 1019–1026.

59 P. Dauber-Osguthorpe, V. A. Roberts, D. J. Osguthorpe, J. Wolff, M. Genest and A. T. Hagler, *Proteins*, 1988, **4**, 31–47.

60 A. P. Thompson, H. M. Aktulga, R. Berger, D. S. Bolintineanu, W. M. Brown, P. S. Crozier, P. J. in't Veld, A. Kohlmeyer, S. G. Moore, T. D. Nguyen, R. Shan, M. J. Stevens, J. Tranchida, C. Trott and S. J. Plimpton, *Comput. Phys. Commun.*, 2022, **271**, 108171.

61 M. P. Allen and D. J. Tildesley, *Computer Simulation of Liquids*, Oxford Univ. Press., 2017.

62 D. Marx, *ChemPhysChem*, 2007, **8**, 209–210.

63 T. Dippel, K. D. Kreuer, J. C. Lassègues and D. Rodriguez, *Solid State Ionics*, 1993, **61**, 41–46.

64 M. J. Gillan, D. Alfè and A. Michaelides, *J. Chem. Phys.*, 2016, **144**, 130901.

65 A. D. Boese, *ChemPhysChem*, 2015, **16**, 978–985.

66 A. Simon and G. Schulze, *Z. Anorg. Allg. Chem.*, 1939, **242**, 313–368.

67 Y. A. Fadeeva, I. V. Fedorova, M. A. Krestyaninov and L. P. Safonova, *J. Mol. Liq.*, 2020, **300**, 112342.

68 W. Li, G. Wang and J. Ma, *Natl. Sci. Rev.*, 2023, **10**, nwad335.

